LETTERS
https://doi.org/10.1038/s41567-021-01237-9

nature physics

Quantum amplification of boson-mediated interactions

S. C. Burd[1,2,5]✉, R. Srinivas[1,2,6], H. M. Knaack[1,2], W. Ge[3,7], A. C. Wilson[1], D. J. Wineland[1,2,4], D. Leibfried[1], J. J. Bollinger[1], D. T. C. Allcock[1,2,4] and D. H. Slichter[1]✉

Strong and precisely controlled interactions between quantum objects are essential for quantum information processing[1,2], simulation[3] and sensing[4,5], and for the formation of exotic quantum matter[6]. A well-established paradigm for coupling otherwise weakly interacting quantum objects is to use auxiliary bosonic quantum excitations to mediate the interactions. Important examples include photon-mediated interactions between atoms[7], superconducting qubits[8], and colour centres in diamond[9], and phonon-mediated interactions between trapped ions[10–12] and between optical and microwave photons[13]. Boson-mediated interactions can, in principle, be amplified through parametric driving of the boson channel; the drive need not couple directly to the interacting quantum objects. This technique has been proposed for a variety of quantum platforms[14–24], but has not, so far, been realized in the laboratory. Here we experimentally demonstrate the amplification of a boson-mediated interaction between two trapped-ion qubits by parametric modulation of the trapping potential[21]. The amplification provides up to a 3.25-fold increase in the interaction strength, validated by measuring the speed-up of two-qubit entangling gates. This amplification technique can be used in any quantum platform where parametric modulation of the boson channel is possible, enabling exploration of new parameter regimes and enhanced quantum information processing.

In many experimental platforms for quantum science, interactions between quantum objects are generated by coupling the objects via a shared auxiliary harmonic oscillator degree of freedom. The excitations of the harmonic oscillator are bosons (typically photons or phonons), which mediate interactions between the quantum objects. Such interactions have been used to demonstrate high-fidelity quantum logic gates[25–27], spin-squeezed states of atoms and ions[28–31], and the formation of novel phases of matter[32,33].

Achieving high fidelity generally requires that the effective interaction strength must dominate the characteristic rates of decoherence in the system. Recent theoretical proposals[14–24] offer a way to increase the boson-mediated interaction strength through parametric modulation. When decoherence of the quantum objects to be coupled—including decoherence due to control fields used to implement the coupling[34]—is the primary source of infidelity, this technique can reduce that infidelity by decreasing the required interaction duration. Stronger interactions could also increase speed and reduce control signal power requirements in large-scale quantum processors.

The physics of amplified boson-mediated interactions can be modelled by considering a set of quantum objects with associated operators $\hat{s}_i$ and a collective degree of freedom $\hat{S} \equiv \sum_i \beta_i \hat{s}_i$, with suitable coefficients β_i. This collective degree of freedom is coupled to a harmonic oscillator mode with annihilation and creation operators $\hat{a}$ and $\hat{a}^\dagger$ and frequency ω, which can be parametrically modulated with characteristic strength g at $2\omega + 2\delta$ (δ is a system-dependent frequency offset). In a suitable interaction picture, the corresponding Hamiltonian takes the form[21] (see Methods):

$$\hat{H}_{\mathrm{M}} = \frac{\hbar\Omega_0}{2}(\hat{S}^\dagger \hat{a} + \hat{S}\hat{a}^\dagger) - \hbar\delta\hat{a}^\dagger\hat{a} + \frac{\hbar g}{2}(\hat{a}^2 e^{i\theta} + \hat{a}^{\dagger 2} e^{-i\theta}), \quad (1)$$

where the first two terms describe the unamplified boson-mediated interactions, with coupling strength Ω_0 and detuning δ, and the third term describes the parametric modulation of the boson channel. Here θ is the relative phase between the parametric drive and the coupling interaction in the first term. This general Hamiltonian can be realized in many physical systems including trapped ions[21,22], cavity optomechanics[15] and superconducting circuit quantum electrodynamics or atom–cavity systems[17,18].

For interactions between trapped-ion qubits, the $\hat{a}$ and $\hat{a}^\dagger$ operators typically correspond to a normal mode of ion motion in the trap (whose excitations are phonons) and $\hat{s}_i = \hat{\sigma}_j^i$, where $\hat{\sigma}_j^i$ is a Pauli operator for the ith ion with $j \in \{x, y, z\}$[11,12,35,36]. Here δ is the detuning of the spin-motion coupling drive from the frequency ω of the phonon mode used to implement the interaction, and β_i describes the participation of the ith ion in the phonon mode. As another example, one could also use equation (1) to describe atoms or superconducting qubits coupled to a single electromagnetic field mode in a cavity. There $\hat{a}$ and $\hat{a}^\dagger$ are the cavity mode operators, while $\hat{s}_i = \hat{\sigma}_+^i$, where $\hat{\sigma}_+^i$ is the effective spin-1/2 raising operator for the ith atom in the cavity. The β_i then describes the relative atom–cavity coupling strengths, and δ is the atom–cavity detuning. When $g = 0$, $\hat{H}_{\mathrm{M}}$ is equivalent to the Tavis–Cummings Hamiltonian[37].

As a representative case, we examine the dynamics in a trapped-ion system without parametric modulation ($g = 0$). We consider two trapped-ion qubits (with single-qubit $\hat{\sigma}_z$ eigenstates $|\uparrow\rangle$ and $|\downarrow\rangle$) coupled through a shared out-of-phase mode of motion such that $\hat{S} = \hat{\sigma}_x^1 - \hat{\sigma}_x^2$ (note $\hat{S} = \hat{S}^\dagger$). Applying $\hat{H}_{\mathrm{M}}$ will result in spin-dependent displacements in the phase space of the motional mode[12,36]. The two-qubit spin states $|{+}{+}\rangle$ and $|{-}{-}\rangle$, where $|\pm\rangle \equiv \frac{1}{\sqrt{2}}(|\uparrow\rangle \pm |\downarrow\rangle)$, are not displaced, whereas states $|{+}{-}\rangle$

[1]Time and Frequency Division, National Institute of Standards and Technology, Boulder, CO, USA. [2]Department of Physics, University of Colorado, Boulder, CO, USA. [3]Texas A&M University, College Station, TX, USA. [4]Department of Physics, University of Oregon, Eugene, OR, USA. [5]Present address: Department of Physics, Stanford University, Palo Alto, CA, USA. [6]Present address: Department of Physics, University of Oxford, Oxford, UK. [7]Present address: Department of Physics, Southern Illinois University, Carbondale, IL, USA. ✉e-mail: shaun.burd@colorado.edu; daniel.slichter@nist.gov

and $|-+\rangle$ will traverse circular trajectories in phase space (Fig. 1a), each acquiring a state-dependent geometric phase Φ equal to the area enclosed by its trajectory[12,36]. Applying $\hat{H}_{\mathrm{M}}$ for a duration $\tau = 2\pi/\delta$ returns the harmonic oscillator to its initial state after a single phase-space loop and disentangles it from the spin states. This results in the propagator[38]

$$\hat{U} = \exp\left(i\frac{\Phi}{4}\hat{S}^2\right), \tag{2}$$

which generates an effective spin–spin interaction, where $\Phi = 2\pi(\Omega_0/\delta)^2$. When $\delta = 2\Omega_0$ and $\Phi = \pi/2$ this results in the maximally entangled state: $\hat{U}|\downarrow\downarrow\rangle = \frac{1}{\sqrt{2}}(|\downarrow\downarrow\rangle + i|\uparrow\uparrow\rangle)$. If we include parametric modulation ($g \neq 0$), the dynamics can be elucidated by making the normal mode transformation[39] $\hat{b} \equiv \hat{a}\cosh r - \hat{a}^\dagger e^{i\theta}\sinh r$, where $r = \frac{1}{4}\ln[(\delta+g)/(\delta-g)]$. When $\theta = 0$, this gives

$$\hat{H}_{\mathrm{M}} = \frac{\hbar G\Omega_0}{2}(\hat{S}^\dagger\hat{b} + \hat{S}\hat{b}^\dagger) - \hbar\delta'\hat{b}^\dagger\hat{b}, \tag{3}$$

where $G = [(\delta+g)/(\delta-g)]^{1/4} = e^r$ and $\delta' = \sqrt{\delta^2 - g^2}$, with the requirement that $|\delta| > |g|$. The values of δ and τ depend on Ω_0 and g, and are determined by numerically solving a system of nonlinear equations (see Methods). The transformed Hamiltonian has the mathematical form of a boson-mediated interaction without parametric driving, but the interaction strength has been increased by a factor of G. Similarly, we can derive the propagator as in equation (2), with the duration to acquire a given geometric phase Φ reduced by the same factor of G. The choice of $\theta = 0$ gives the maximum amplification of the interaction strength; other values of θ provide less amplification, or even de-amplification (see Methods). The parametric modulation causes the $|+-\rangle$ and $|-+\rangle$ states to traverse elliptical, rather than circular, trajectories in phase space (Fig. 1b). Physically, the parametric modulation alternately squeezes and anti-squeezes the oscillator wave packets as they follow their elliptical trajectories, resulting in amplification of the spin-dependent displacements[22,40]. For the case where $\hat{S} \neq \hat{S}^\dagger$, the result of parametric modulation depends on the details of $\hat{S}$. For example, in cavity or circuit quantum electrodynamics, the increase in interaction strength is given by $\cosh(r)$, and the amplification is independent of θ, as shown in ref. [17].

In our experiment, we amplify boson-mediated interactions between two trapped $^{25}Mg^+$ ion hyperfine qubits. The ions are held ~30 μm above a linear surface-electrode radio-frequency trap[40–42] operated at 15 K. The harmonic oscillator mode is an out-of-phase radial motional mode with frequency $\omega \simeq 2\pi \times 5.9$ MHz. We use qubit states $|\downarrow\rangle \equiv |F = 3, m_F = 1\rangle$ and $|\uparrow\rangle \equiv |F = 2, m_F = 1\rangle$ within the $^2S_{1/2}$ electronic ground state hyperfine manifold, where F is the total angular momentum and m_F is its projection along the quantization axis defined by a 21.3 mT magnetic field. At this field strength, the qubit transition frequency $\omega_0 \simeq 2\pi \times 1.686$ GHz is insensitive to magnetic field fluctuations to first order, resulting in a qubit coherence time longer than 200 ms. Global qubit rotations and coherent population transfer between hyperfine states as required for state preparation and readout are performed by applying resonant microwave pulses to trap electrodes.

In each experiment, the ions are initialized in the electronic ground state $|\downarrow\downarrow\rangle$, and close to the motional ground state (mean occupation $\bar{n} \approx 0.3$ in the phonon mode used to mediate interactions), with optical pumping, resolved-sideband laser cooling[43] and microwave pulses. Qubit readout is accomplished by transferring the population in $|\downarrow\rangle$ to $^2S_{1/2}|F = 3, m_F = 3\rangle$, applying a laser resonant with the $^2S_{1/2}|F = 3, m_F = 3\rangle \leftrightarrow {}^2P_{3/2}|F = 4, m_F = 4\rangle$ cycling transition, and detecting state-dependent ion fluorescence. Coupling between qubits and phonons associated with the shared motional mode is implemented using the Mølmer–Sørensen (MS) interaction[11,38]. We implement the MS interaction using oscillating near-field magnetic field gradients at $\omega_0 \pm (\omega + \delta)$, generated by currents in the trap electrodes (see Methods)[44,45]. We measure $\Omega_0/2\pi = 1.46(1)$ kHz, corresponding to a nominal single-loop MS gate duration ($\tau = \pi/\Omega_0$) of 342(3) μs. Generating the MS interaction in this way enables straightforward phase synchronization with the parametric modulation at $2\omega + 2\delta$, which is implemented by applying an oscillating potential directly to the radio-frequency trapping electrodes as described in ref. [40].

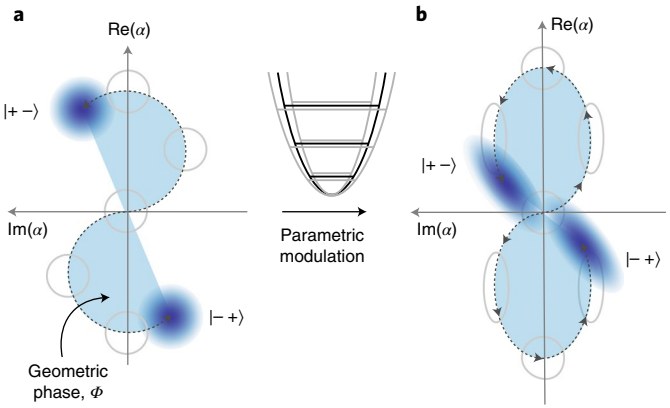

Fig. 1 | Phase-space illustration of boson-mediated interactions. We show the dimensionless complex harmonic oscillator amplitude α and corresponding schematic quasi-probability distributions[7] (shown in dark blue, with past positions outlined in grey) for two qubits ($\hat{S} = \hat{\sigma}_x^1 - \hat{\sigma}_x^2$) assumed to be initialized at the origin of phase space. In both panels, the interaction duration is the same. **a**, Without parametric modulation ($g = 0$), the wave packets associated with the $|+-\rangle$ and $|-+\rangle$ spin states follow circular trajectories in a frame rotating at $\omega + \delta$. The enclosed area (shown in light blue) is equal to the acquired geometric phase Φ. **b**, With parametric modulation of the trap potential at $2\omega + 2\delta$, the trajectories (again viewed in a frame rotating at $\omega + \delta$) become elliptical and the motional wave packets are alternately squeezed and anti-squeezed. The parametric modulation results in increased geometric phase being acquired per unit time.

To quantify the enhancement in the interaction strength due to parametric amplification, we find, for a given parametric coupling strength g, the optimum interaction duration for preparing the Bell state $|\psi_{\mathrm{B}}\rangle = \frac{1}{\sqrt{2}}(|\downarrow\downarrow\rangle + i|\uparrow\uparrow\rangle)$ from the initial state $|\downarrow\downarrow\rangle$. In the absence of decoherence, this corresponds to acquiring a geometric phase of $\Phi = \pi/2$, using a single phase-space loop. To determine the optimal interaction duration we perform measurements for different values of the interaction duration t_{I} and detuning δ' at each g, and use the fidelity $F(g, t_{\mathrm{I}}, \delta') = \langle\psi_{\mathrm{B}}|\hat{\rho}(g, t_{\mathrm{I}}, \delta')|\psi_{\mathrm{B}}\rangle$ of the prepared state as a success metric, where $\hat{\rho}$ is the density matrix of the prepared state[46]. For each g, we perform a two-dimensional (2D) quadratic fit to the measured fidelity values versus t_{I} and δ' and use the t_{I} value of the fit function maximum as the estimated optimal interaction duration $\tilde{t}_{\mathrm{I,est}}$ (see Methods and Extended Data Fig. 1). With $t_0 \equiv \tilde{t}_{\mathrm{I,est}}(g = 0) = 331(1)$ μs denoting the estimated optimal interaction duration without parametric amplification, we plot the measured gate speed-up $t_0/\tilde{t}_{\mathrm{I,est}}$ versus g in Fig. 2a. The values of $\tilde{t}_{\mathrm{I,est}}$ tend to be shorter than predicted by analytical theory without decoherence. This effect arises from a trade-off between fidelity reductions from amplified motional decoherence (which penalize longer t_{I}) and fidelity reductions from incorrect geometric phase acquisition or failure to close the phase-space loop (which penalize t_{I} either shorter or longer than the optimal duration without decoherence). The measured $\tilde{t}_{\mathrm{I,est}}$ values agree quantitatively with numerical simulations incorporating motional heating and dephasing mechanisms.

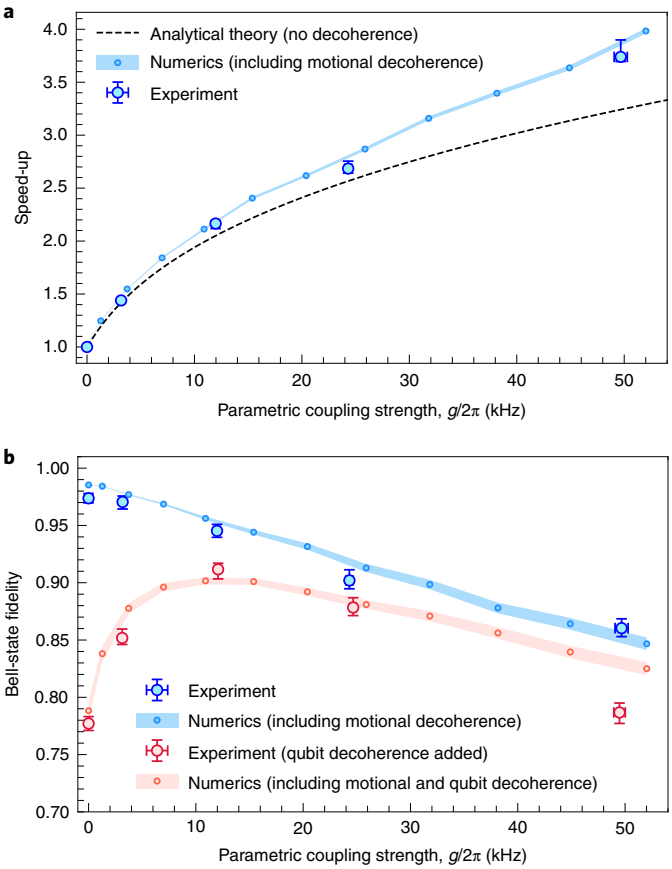

Fig. 2 | Bell-state fidelities and speed-up. a, Speed-up $t_0/\tilde{t}_{l,est}$ as a function of g. The dashed line is the prediction from analytical theory without motional decoherence. The small points are the results of numerical simulations including motional decoherence, with the coloured bands representing the corresponding 68% confidence intervals, linearly interpolated between simulated points[21]. **b**, Bell-state fidelities with and without added qubit dephasing. We plot $\tilde{F}_{exp}$, the maximum measured fidelity for each value of g, determined by scanning over a 2D grid of interaction times t_l and detunings δ'. Red circles (blue circles) indicate data taken with (without) added qubit dephasing noise (see text and Methods). Small points show numerical simulations of the maximum fidelity (varying t_l and δ') as a function of g, including motional decoherence, and either with (red) or without (blue) added qubit decoherence. The coloured bands represent 68% confidence intervals on the numerically simulated values, linearly interpolated between simulated points. In **a** and **b**, experimental error bars indicate 68% confidence intervals.

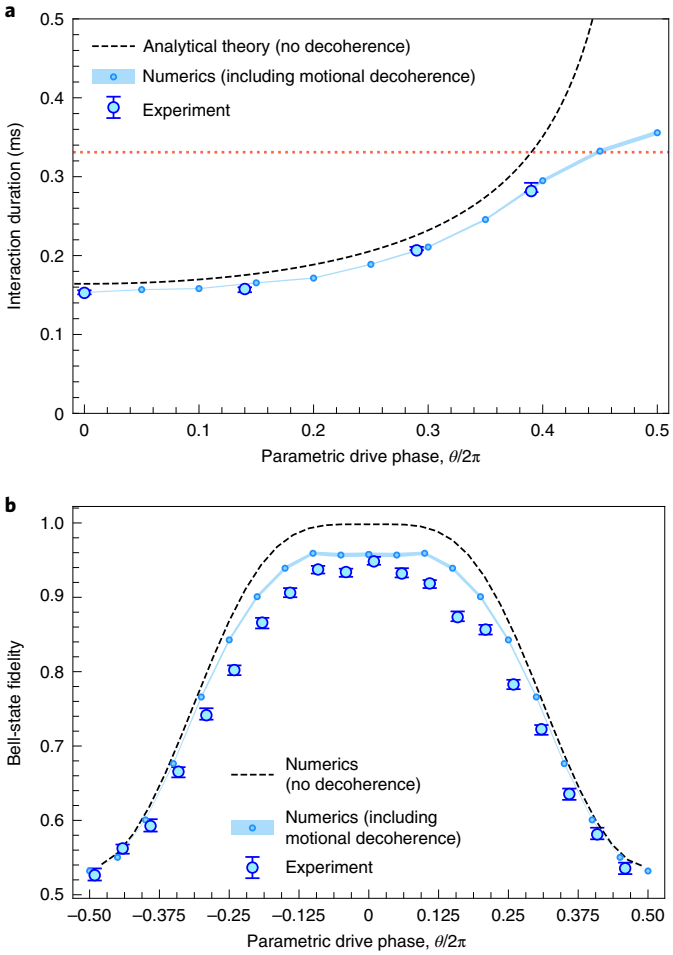

Fig. 3 | Phase dependence of amplification. a, Interaction duration $\tilde{t}_{l,est}$ as a function of the parametric drive phase θ for $g=2\pi\times12.4(2)$ kHz. The dotted red line indicates the duration t_0 without parametric amplification. The dashed black line is from analytical theory, without considering decoherence. **b**, Fidelity as a function of θ for fixed g, t_l and δ, with t_l and δ chosen to maximize fidelity at $\theta=0$ for $g=2\pi\times12.4(2)$ kHz. The dashed black line is from numerical simulation, without considering decoherence. In **a** and **b**, the small points are the result of numerical simulations including motional decoherence (see Methods), with the coloured bands representing the 68% confidence intervals, linearly interpolated between simulated points, and the error bars on experimental data indicate 68% confidence intervals.

For the strongest parametric coupling of $g=2\pi\times49.7(6)$ kHz, we experimentally measure a speed-up factor of $3.74^{+0.16}_{-0.04}$. With this g and the independently calibrated Ω_0, we calculate a theoretical enhancement in the phonon-mediated interaction strength of $G=3.25(1)$ (see Methods).

The amplified motional decoherence also causes the interaction fidelity to diminish as g is increased. We define the maximum experimentally measured fidelity $\tilde{F}_{exp}(g)$ for a given g (scanning over δ' and t_l, see Methods) and plot $\tilde{F}_{exp}$ for each g in Fig. 2b. For a parametric coupling strength of $g=2\pi\times49.7(6)$ kHz, we measure $\tilde{F}_{exp}=0.860(8)$ for $t_l=90\,\mu s$, compared with $\tilde{F}_{exp}=0.974(4)$ without parametric amplification at $t_l=350\,\mu s$.

In our experiment, decoherence of the shared boson mode (ion motion) is the dominant source of gate infidelity. However, decoherence mechanisms not arising from the shared boson mode (for example, off-resonant photon scattering from laser control fields[34,47]) are not amplified; in cases where these are the dominant source of infidelity, parametric amplification may improve the interaction fidelity by reducing the interaction duration[21]. As a proof-of-principle demonstration of operation in this regime, we introduce excess qubit dephasing by applying a current oscillating near ω_0 to one of the trap electrodes. The detuned current gives rise to an ac Zeeman shift of the qubit frequency. The amplitude of the current is randomly changed every millisecond to give a Gaussian distribution (standard deviation of $2\pi\times0.47(2)$ kHz, see Methods) of qubit frequency shifts in time. In the presence of this dephasing, the maximum $\tilde{F}_{exp}$ without parametric modulation is 0.777(6), at $t_l=310\,\mu s$, whereas with parametric modulation ($g=2\pi\times12.1(1)$ kHz) we measure a maximum $\tilde{F}_{exp}$ of 0.912(7) at $t_l=160\,\mu s$ (Fig. 2b red points). Further increases in g reduce the fidelity, due to amplified motional decoherence.

In the experiments described above, the phase θ of the parametric drive with respect to the MS fields was set to give maximum

amplification ($\theta=0$). We can also vary θ to study the phase sensitivity of the amplification protocol. In Fig. 3a, we determine $\tilde{t}_{1,\mathrm{est}}$ for different θ values and a fixed $g=2\pi\times12.4(2)$ kHz by scanning over multiple (t_1, δ') pairs for each data point, as described above. Theoretically, the parametric amplification process is third-order insensitive to small errors in the parametric drive phase[21], and we measure no substantial increase in $\tilde{t}_{1,\mathrm{est}}$ up to at least $\theta/2\pi\approx0.14$. Increasing θ further results in a longer $\tilde{t}_{1,\mathrm{est}}$, in accordance with theoretical predictions. The increased $\tilde{t}_{1,\mathrm{est}}$ is accompanied by a reduction in the maximum value of $\tilde{F}_{\mathrm{exp}}$ over t_1 for each phase value, going from 0.945(6) to 0.738(8) as $\theta/2\pi$ changes from 0 to 0.39. Simulations show that this fidelity loss is due to parametric amplification of motional decoherence. In Fig. 3b, we show the effect of varying θ for the same fixed g, this time without reoptimizing the gate parameters δ' and t_1 for each θ. Although in our system the control fields used to induce boson-mediated interactions are at microwave frequencies and can therefore be readily phase-stabilized with respect to the parametric drive, applications with laser-based control fields may require stabilization of the laser optical phase at the ion positions relative to the parametric drive phase. The fact that the interaction duration and fidelity are not first-order sensitive to this phase difference eases the requirements for the laser phase stability.

In summary, we have demonstrated parametric amplification of boson-mediated interactions between two trapped-ion qubits. Our method should increase entangling-gate fidelities in systems where the dominant sources of error result from qubit decoherence or from qubit errors induced by control fields, rather than decoherence of the bosonic degree of freedom that couples the qubits. The loss of fidelity due to amplified decoherence of the boson mode could potentially be mitigated by using multiple phase-space loops[48], or using multi-tone or amplitude-modulated schemes[49–53]. Furthermore, the enhanced interaction strength afforded by parametric amplification could enable a reduction in the amount of laser or microwave power required in larger-scale quantum information processors.

Online content

Any methods, additional references, Nature Research reporting summaries, source data, extended data, supplementary information, acknowledgements, peer review information; details of author contributions and competing interests; and statements of data and code availability are available at https://doi.org/10.1038/s41567-021-01237-9.

Received: 13 October 2020; Accepted: 1 April 2021;
Published online: 13 May 2021

References

1. Bruzewicz, C. D., Chiaverini, J., McConnell, R. & Sage, J. M. Trapped-ion quantum computing: progress and challenges. *Appl. Phys. Rev.* **6**, 021314 (2019).
2. Blais, A., Girvin, S. M. & Oliver, W. D. Quantum information processing and quantum optics with circuit quantum electrodynamics. *Nat. Phys.* **16**, 247–256 (2020).
3. Georgescu, I. M., Ashhab, S. & Nori, F. Quantum simulation. *Rev. Mod. Phys.* **86**, 153–185 (2014).
4. Degen, C. L., Reinhard, F. & Cappellaro, P. Quantum sensing. *Rev. Mod. Phys.* **89**, 035002 (2017).
5. Pezzè, L., Smerzi, A., Oberthaler, M. K., Schmied, R. & Treutlein, P. Quantum metrology with nonclassical states of atomic ensembles. *Rev. Mod. Phys.* **90**, 035005 (2018).
6. Bloch, I., Dalibard, J. & Zwerger, W. Many-body physics with ultracold gases. *Rev. Mod. Phys.* **80**, 885–964 (2008).
7. Gerry, C. C. & Knight, P. L. *Introductory Quantum Optics* (Cambridge Univ. Press, 2005).
8. Blais, A., Huang, R.-S., Wallraff, A., Girvin, S. M. & Schoelkopf, R. J. Cavity quantum electrodynamics for superconducting electrical circuits: an architecture for quantum computation. *Phys. Rev. A* **69**, 062320 (2004).
9. Evans, R. E. et al. Photon-mediated interactions between quantum emitters in a diamond nanocavity. *Science* **362**, 662–665 (2018).
10. Cirac, J. I. & Zoller, P. Quantum computations with cold trapped ions. *Phys. Rev. Lett.* **74**, 4091–4094 (1995).
11. Sørensen, A. & Mølmer, K. Quantum computation with ions in thermal motion. *Phys. Rev. Lett.* **82**, 1971–1974 (1999).
12. Milburn, G. J., Schneider, S. & James, D. F. V. Ion trap quantum computing with warm ions. *Fortschr. Phys.* **48**, 801–810 (2000).
13. Higginbotham, A. P. et al. Harnessing electro-optic correlations in an efficient mechanical converter. *Nat. Phys.* **14**, 1038–1042 (2018).
14. Lü, X.-Y. et al. Squeezed optomechanics with phase-matched amplification and dissipation. *Phys. Rev. Lett.* **114**, 093602 (2015).
15. Lemonde, M.-A., Didier, N. & Clerk, A. A. Enhanced nonlinear interactions in quantum optomechanics via mechanical amplification. *Nat. Commun.* **7**, 11338 (2016).
16. Zeytinoğlu, S., İmamoğlu, A. & Huber, S. Engineering matter interactions using squeezed vacuum. *Phys. Rev. X* **7**, 021041 (2017).
17. Qin, W. et al. Exponentially enhanced light-matter interaction, cooperativities, and steady-state entanglement using parametric amplification. *Phys. Rev. Lett.* **120**, 093601 (2018).
18. Chen, Y.-H., Qin, W. & Nori, F. Fast and high-fidelity generation of steady-state entanglement using pulse modulation and parametric amplification. *Phys. Rev. A* **100**, 012339 (2019).
19. Leroux, C., Govia, L. C. G. & Clerk, A. A. Enhancing cavity quantum electrodynamics via antisqueezing: synthetic ultrastrong coupling. *Phys. Rev. Lett.* **120**, 093602 (2018).
20. Arenz, C., Bondar, D. I., Burgarth, D., Cormick, C. & Rabitz, H. Amplification of quadratic Hamiltonians. *Quantum* **4**, 271 (2020).
21. Ge, W. et al. Trapped ion quantum information processing with squeezed phonons. *Phys. Rev. Lett.* **122**, 030501 (2019).
22. Ge, W. et al. Stroboscopic approach to trapped-ion quantum information processing with squeezed phonons. *Phys. Rev. A* **100**, 043417 (2019).
23. Groszkowski, P., Lau, H.-K., Leroux, C., Govia, L. C. G. & Clerk, A. A. Heisenberg-limited spin squeezing via bosonic parametric driving. *Phys. Rev. Lett.* **125**, 203601 (2020).
24. Li, P.-B., Zhou, Y., Gao, W.-B. & Nori, F. Enhancing spin-phonon and spin-spin interactions using linear resources in a hybrid quantum system. *Phys. Rev. Lett.* **125**, 153602 (2020).
25. Ballance, C. J., Harty, T. P., Linke, N. M., Sepiol, M. A. & Lucas, D. M. High-fidelity quantum logic gates using trapped-ion hyperfine qubits. *Phys. Rev. Lett.* **117**, 060504 (2016).
26. Gaebler, J. P. et al. High-fidelity universal gate set for $^{9}Be^{+}$ ion qubits. *Phys. Rev. Lett.* **117**, 060505 (2016).
27. McKay, D. C., Sheldon, S., Smolin, J. A., Chow, J. M. & Gambetta, J. M. Three-qubit randomized benchmarking. *Phys. Rev. Lett.* **122**, 200502 (2019).
28. Meyer, V. et al. Experimental demonstration of entanglement-enhanced rotation angle estimation using trapped ions. *Phys. Rev. Lett.* **86**, 5870–5873 (2001).
29. Cox, K. C., Greve, G. P., Weiner, J. M. & Thompson, J. K. Deterministic squeezed states with collective measurements and feedback. *Phys. Rev. Lett.* **116**, 093602 (2016).
30. Hosten, O., Engelsen, N. J., Krishnakumar, R. & Kasevich, M. A. Measurement noise 100 times lower than the quantum-projection limit using entangled atoms. *Nature* **529**, 505–508 (2016).
31. Bohnet, J. G. et al. Quantum spin dynamics and entanglement generation with hundreds of trapped ions. *Science* **352**, 1297–1301 (2016).
32. Mottl, R. et al. Roton-type mode softening in a quantum gas with cavity-mediated long-range interactions. *Science* **336**, 1570–1573 (2012).
33. Léonard, J., Morales, A., Zupancic, P., Esslinger, T. & Donner, T. Supersolid formation in a quantum gas breaking a continuous translational symmetry. *Nature* **543**, 87–90 (2017).
34. Ozeri, R. et al. Errors in trapped-ion quantum gates due to spontaneous photon scattering. *Phys. Rev. A* **75**, 042329 (2007).
35. Sackett, C. A. et al. Experimental entanglement of four particles. *Nature* **404**, 256–259 (2000).
36. Leibfried, D. et al. Experimental demonstration of a robust, high-fidelity geometric two ion-qubit phase gate. *Nature* **422**, 412–415 (2003).
37. Tavis, M. & Cummings, F. W. Exact solution for an *n*-molecule—radiation-field Hamiltonian. *Phys. Rev.* **170**, 379–384 (1968).
38. Mølmer, K. & Sørensen, A. Multiparticle entanglement of hot trapped ions. *Phys. Rev. Lett.* **82**, 1835–1838 (1999).
39. Bogoljubov, N. N. On a new method in the theory of superconductivity. *Nuovo Cimento* **7**, 794–805 (1958).
40. Burd, S. C. et al. Quantum amplification of mechanical oscillator motion. *Science* **364**, 1163–1165 (2019).
41. Seidelin, S. et al. Microfabricated surface-electrode ion trap for scalable quantum information processing. *Phys. Rev. Lett.* **96**, 253003 (2006).
42. Srinivas, R. et al. Trapped-ion spin-motion coupling with microwaves and a near-motional oscillating magnetic field gradient. *Phys. Rev. Lett.* **122**, 163201 (2019).

43. Monroe, C. et al. Resolved-sideband Raman cooling of a bound atom to the 3D zero-point energy. *Phys. Rev. Lett.* **75**, 4011–4014 (1995).
44. Ospelkaus, C. et al. Trapped-ion quantum logic gates based on oscillating magnetic fields. *Phys. Rev. Lett.* **101**, 090502 (2008).
45. Ospelkaus, C. et al. Microwave quantum logic gates for trapped ions. *Nature* **476**, 181–184 (2011).
46. Keith, A. C., Baldwin, C. H., Glancy, S. & Knill, E. Joint quantum-state and measurement tomography with incomplete measurements. *Phys. Rev. A* **98**, 042318 (2018).
47. Uys, H. et al. Decoherence due to elastic Rayleigh scattering. *Phys. Rev. Lett.* **105**, 200401 (2010).
48. Sørensen, A. & Mølmer, K. Entanglement and quantum computation with ions in thermal motion. *Phys. Rev. A* **62**, 022311 (2000).
49. Haddadfarshi, F. & Mintert, F. High fidelity quantum gates of trapped ions in the presence of motional heating. *New J. Phys.* **18**, 123007 (2016).
50. Webb, A. E. et al. Resilient entangling gates for trapped ions. *Phys. Rev. Lett.* **121**, 180501 (2018).
51. Shapira, Y., Shaniv, R., Manovitz, T., Akerman, N. & Ozeri, R. Robust entanglement gates for trapped-ion qubits. *Phys. Rev. Lett.* **121**, 180502 (2018).
52. Zarantonello, G. et al. Robust and resource-efficient microwave near-field entangling $^{9}Be^{+}$ gate. *Phys. Rev. Lett.* **123**, 260503 (2019).
53. Sutherland, R. T. et al. Laser-free trapped-ion entangling gates with simultaneous insensitivity to qubit and motional decoherence. *Phys. Rev. A* **101**, 042334 (2020).

Methods

Derivation of equation (1) for combined MS interaction and parametric modulation. Here we show explicitly that the combined MS and parametric interactions can be described by equation (1). We consider two co-trapped atomic ions with internal qubit states $|\downarrow\rangle$ and $|\uparrow\rangle$ with energy separation $\hbar\omega_0$. Interactions between the qubits are mediated by a shared out-of-phase motional mode with frequency ω. Without driving fields, the lab-frame Hamiltonian for the system is given by[54]

$$\hat{H}_0 = \hbar\omega\hat{a}^\dagger\hat{a} + \frac{\hbar\omega_0}{2}(\hat{\sigma}_z^1 + \hat{\sigma}_z^2), \tag{4}$$

where $\hat{\sigma}_z^i = |\uparrow\rangle\langle\uparrow| - |\downarrow\rangle\langle\downarrow|$ is a Pauli operator for ion i and $\hat{a}$ ($\hat{a}^\dagger$) is the annihilation (creation) operator for the phonon mode. The MS interaction is implemented by simultaneously applying red sideband (RSB) and blue sideband (BSB) interactions[11]

$$\begin{aligned}\hat{H}_{\mathrm{MS}} &= \hat{H}_{\mathrm{BSB}} + \hat{H}_{\mathrm{RSB}} \\ &= \hbar\Omega_0(\hat{\sigma}_+^1 - \hat{\sigma}_+^2)\hat{a}^\dagger\cos(\omega_{\mathrm{BSB}}t) \\ &\quad + \hbar\Omega_0(\hat{\sigma}_+^1 - \hat{\sigma}_+^2)\hat{a}\cos(\omega_{\mathrm{RSB}}t) + \text{ h.c.},\end{aligned} \tag{5}$$

where h.c. is the Hermitian conjugate, Ω_0 characterizes the qubit-motion coupling strength, and ω_{BSB} and ω_{RSB} are the frequencies of the sideband drives. If the sideband drives are symmetrically detuned from ω_0 such that $\omega_{\mathrm{BSB}} = \omega_0 + \omega + \delta$, and $\omega_{\mathrm{RSB}} = \omega_0 - \omega - \delta$, we can transform into an interaction picture with respect to $\hat{H}_0$ to obtain[11]

$$\begin{aligned}\hat{H}_{\mathrm{MS_I}} &= e^{i\hat{H}_0 t/\hbar}\hat{H}_{\mathrm{MS}}e^{-i\hat{H}_0 t/\hbar} \\ &= \tfrac{\hbar\Omega_0}{2}(\hat{a}e^{+i\delta t} + \hat{a}^\dagger e^{-i\delta t})(\hat{\sigma}_x^1 - \hat{\sigma}_x^2),\end{aligned} \tag{6}$$

where we have made a rotating wave approximation and dropped terms oscillating near $2\omega_0$. The minus sign between the Pauli operators arises because the shared motional mode is an out-of-phase mode ($\beta_1 = -\beta_2 = 1$, recalling the definition $\hat{S} \equiv \sum_i \beta_i \hat{s}_i$, where here $\hat{s}_i = \hat{\sigma}_x^i$).

We now consider the parametric drive. In the lab frame, modulation of the confining potential of a trapped-ion mechanical oscillator at frequency ω_{P} results in the Hamiltonian[55]

$$\hat{H}_{\mathrm{P}} = \hbar g(\hat{a} + \hat{a}^\dagger)^2\cos(\omega_{\mathrm{P}}t + \theta), \tag{7}$$

where g is the parametric coupling strength and θ is the phase of the parametric drive relative to the MS interaction fields. If $\omega_{\mathrm{P}} = 2\omega + 2\delta$, then the parametric drive Hamiltonian, in the interaction picture with respect to $\hat{H}_0$ and after making a rotating wave approximation, becomes

$$\hat{H}_{\mathrm{P_I}} = \frac{\hbar g}{2}(\hat{a}^2 e^{2i\delta t + i\theta} + \hat{a}^{\dagger 2}e^{-2i\delta t - i\theta}). \tag{8}$$

Applying the MS fields and parametric drive simultaneously yields:

$$\begin{aligned}\hat{H}_{\mathrm{I}} &= \hat{H}_{\mathrm{MS_I}} + \hat{H}_{\mathrm{P_I}} \\ &= \tfrac{\hbar\Omega_0}{2}(\hat{a}e^{i\delta t} + \hat{a}^\dagger e^{-i\delta t})(\hat{\sigma}_x^1 - \hat{\sigma}_x^2) \\ &\quad + \tfrac{\hbar g}{2}(\hat{a}^2 e^{2i\delta t + i\theta} + \hat{a}^{\dagger 2}e^{-2i\delta t - i\theta}).\end{aligned} \tag{9}$$

If we transform equation (9) into the interaction picture with respect to $\hat{H}_1 = \hbar\delta\hat{a}^\dagger\hat{a}$, the time dependence can be eliminated, giving

$$\begin{aligned}e^{i\frac{\hat{H}_1 t}{\hbar}}\hat{H}_{\mathrm{I}}e^{-i\frac{\hat{H}_1 t}{\hbar}} &= \tfrac{\hbar\Omega_0}{2}(\hat{a} + \hat{a}^\dagger)(\hat{\sigma}_x^1 - \hat{\sigma}_x^2) \\ &\quad + \tfrac{\hbar g}{2}(\hat{a}^2 e^{i\theta} + \hat{a}^{\dagger 2}e^{-i\theta}) - \hbar\delta\hat{a}^\dagger\hat{a},\end{aligned} \tag{10}$$

which is equivalent to equation (1) with $\hat{S} = \hat{\sigma}_x^1 - \hat{\sigma}_x^2$, using the fact that $\hat{S} = \hat{S}^\dagger$ by this definition.

Phase dependence of parametric amplification. Applying the normal mode (Bogoliubov) transformation[39] $\hat{b} \equiv \hat{a}\cosh r - \hat{a}^\dagger e^{i\theta}\sinh r$ to equation (1) gives the expression

$$\begin{aligned}\hat{H}_{\mathrm{M}} &= \tfrac{\hbar\Omega_0}{2}\left(\hat{S}^\dagger\left[\hat{b}\cosh r + \hat{b}^\dagger e^{i\theta}\sinh r\right]\right. \\ &\quad \left. + \hat{S}\left[\hat{b}^\dagger\cosh r + \hat{b}\,e^{-i\theta}\sinh r\right]\right) - \hbar\delta'\hat{b}^\dagger\hat{b},\end{aligned} \tag{11}$$

where $r = \frac{1}{4}\ln\left[(\delta + g)/(\delta - g)\right]$ and $\delta' = \sqrt{\delta^2 - g^2}$, with the requirement that $|\delta| > |g|$ and $\delta, g \geq 0$. For cases where $\hat{S} = \hat{S}^\dagger$, we have

$$\hat{H}_{\mathrm{M}} = \frac{\hbar\Omega_0}{2}\hat{S}\left(\hat{b}f(r,\theta) + \hat{b}^\dagger f^*(r,\theta)\right) - \hbar\delta'\hat{b}^\dagger\hat{b}, \tag{12}$$

where $f(r,\theta) = \cosh r + e^{i\theta}\sinh r$. The interaction strength Ω_0 is modified by a factor $|f(r,\theta)|$ (the phase of f can be absorbed into the $\hat{b}$ operator), which is given by

$$|f(r,\theta)| = \sqrt{\cosh 2r + \cos\theta\sinh 2r}. \tag{13}$$

Maximum amplification occurs when $\theta = 0$, when $|f(r,0)| = e^r$ and the interaction strength becomes $\Omega_0 e^r$. If $\theta = \pi$, the interaction strength is maximally suppressed, with $|f(r,\pi)| = e^{-r}$ and $\Omega_0 \to \Omega_0 e^{-r}$. Equation (13) can be reparameterized in terms of δ and g to give:

$$|f(\delta, g, \theta)| = \left|\frac{\delta + g\cos(\theta)}{\sqrt{\delta^2 - g^2}}\right|^{1/2}, \tag{14}$$

for $\delta > 0$. The above analysis also holds if $\delta < 0$ (we always presume $g \geq 0$), provided that a phase shift of π is added to θ as well.

Calculation of the gate time and detuning for parametrically amplified gates without decoherence. The preparation of the Bell state $|\psi_{\mathrm{B}}\rangle = \frac{1}{\sqrt{2}}(|\downarrow\downarrow\rangle + i|\uparrow\uparrow\rangle)$ from the initial state $|\downarrow\downarrow\rangle$ requires the closure of an integer number of phase-space loops and the accumulation of a geometric phase of $\Phi = \pi/2$. The closure of a single loop occurs when τ is given by:

$$\tau = \frac{2\pi}{\delta'} = \frac{2\pi}{\sqrt{\delta^2 - g^2}}. \tag{15}$$

The geometric phase acquired in that loop, Φ, is:

$$\Phi = 2\pi\left(\frac{\Omega_0|f(g,\delta,\theta)|}{\delta'}\right)^2 = 2\pi\left(\frac{\Omega_0|f(g,\delta,\theta)|}{\sqrt{\delta^2 - g^2}}\right)^2. \tag{16}$$

Given g, θ and Ω_0, we can determine the correct values of τ and δ by numerically solving equations (15) and (16) simultaneously. All values of τ from analytical theory shown in the text are calculated in this manner.

Calibration of the parametric drive strength g. The electronics used to generate the parametric drive are described in detail in ref. [40] and consist of a direct digital synthesizer driving a resonant tank circuit coupled to the trap radio-frequency electrodes. Since a resonant circuit is used to couple the parametric drive to the trap electrodes, the parametric drive strength g depends on the frequency ω_{P}. During entangling-gate experiments there are both slow drifts of the ion mode frequency ω and deliberate changes to the detuning δ. These result in small changes in g, since $\omega_{\mathrm{P}} = 2\omega + 2\delta$. Since we measured ω at the beginning of every gate experiment, we can infer the value of g for that experiment using an independently measured calibration function.

For given settings of the mode frequency ω and parametric drive amplitude, we measured g using a similar method to that described in ref. [40]. First, we prepared the two-ion state $|\uparrow\uparrow\rangle$, with the motion cooled near the ground state ($\bar{n} \approx 0.3$). Next, we squeezed the motional state by applying the parametric drive on-resonance (with $\omega_{\mathrm{P}} = 2\omega$) for a duration t. Parametric modulation ideally implements a squeezing operation[40,55,56], and transforms the motional density matrix $\hat{\rho}_{\mathrm{i}}$ according to

$$\hat{\rho}_{\mathrm{s}} = \hat{Q}(\xi)\hat{\rho}_{\mathrm{i}}\hat{Q}^\dagger(\xi), \tag{17}$$

where $\hat{\rho}_{\mathrm{s}}$ is the squeezed motional density matrix and $\hat{Q}(\xi) = \exp\left(\frac{1}{2}\left(\xi^*\hat{a}^2 - \xi\hat{a}^{\dagger 2}\right)\right)$ is the squeezing operator with complex squeezing parameter $\xi = gte^{i\theta}$. The initial density matrix $\hat{\rho}_{\mathrm{i}}$ is assumed to be in a thermal mixed state characterized by the mean thermal occupation $\bar{n}$. The oscillator number state populations of the shared two-ion motional state can be inferred from the ions' qubit populations after applying a motion-adding sideband pulse of a variable duration and detecting the two-ion qubit populations. We can extract the value of $|\xi|$, and hence g, by fitting a numerical model to the measured two-ion populations as a function of the duration of the sideband pulse, with only $|\xi|$ as a free parameter. Additional parameters used in the model are the sideband Rabi frequency for each ion, the ac Zeeman shift on each ion due to off-resonant magnetic fields associated with the sideband drive, and $\bar{n}$, which are calibrated by fitting the model to data from a control experiment with the parametric drive amplitude set to zero. We repeated this experiment for various values of ω and fit a quadratic polynomial to the resulting data, obtaining a calibration function for g as a function of ω. All reported uncertainty values for g are 68% functional prediction intervals[57] based on this calibration function fit. The prediction interval reflects our uncertainty in determining the underlying value of g, but not fluctuations of g in time for a given ω, which are substantially smaller.

Determination of $\tilde{t}_{\mathrm{I,est}}$. For a given setting of the parametric drive amplitude g, we estimated the interaction duration required to maximize the two-qubit gate fidelity by fitting a 2D quadratic polynomial to the data. Specifically, we fit to a

grid of experimentally measured fidelities at various (t_l,δ) values to determine the quadratic constants a_i in the function

$$F(x,y) = a_0 + a_1(x-a_4)^2 + a_2(y-a_5)^2 + a_3(x-a_4)(y-a_5), \quad (18)$$

with $x \equiv t_l$, and $y \equiv \delta'$. This requires converting the experimentally measured δ values into δ' values, which requires knowledge of g. Any calibration uncertainty in g will propagate to the values of δ'. The fitted value of the coefficient a_4 gives $\tilde{t}_{l,est}$. Data and slices of the 2D fit for the point at $g = 2\pi \times 49.7(6)$ kHz in Fig. 2a are shown in Extended Data Fig. 1. From the fit, $\tilde{t}_{l,est} = 88^{+1}_{-3}$ µs.

To determine the effect of the calibration uncertainty in g on $\tilde{t}_{l,est}$ (arising from the propagation of this uncertainty into the δ' values), as well as the uncertainty in the estimated fidelities, we used bootstrapping. For each setting of the parametric coupling strength, we generated 5,000 synthetic data sets, each with the same number of (t_l, δ') data points as in the original data set. Each point in a new set has the original duration t_l, but has a detuning given by $\delta' = \sqrt{\delta^2 - (g + \Delta g)^2}$, where Δg is randomly selected from a zero-mean Gaussian distribution with standard deviation given by the calibration uncertainty in g ($\sim 2\pi \times 600$ Hz for the data shown in Extended Data Fig. 1). Similarly, the fidelity values F are given by $F + \Delta F$, where ΔF is randomly selected from a zero-mean Gaussian distribution with standard deviation given by the standard deviation of estimated fidelities from non-parametric bootstrapping of the raw gate data[46]. For each synthetic data set we fit $F(x,y)$ to the data to determine $\tilde{t}_{l,est}$, and used the central 68% interval of the distribution of fitted values to determine the uncertainty in $\tilde{t}_{l,est}$.

Excess qubit dephasing noise. The $|{\downarrow}\rangle \leftrightarrow |{\uparrow}\rangle$ transition frequency is first-order insensitive to magnetic field fluctuations (a so-called clock transition). We therefore induced excess qubit frequency fluctuations, and thus dephasing, by applying a time-varying ac Zeeman shift δ_{ac}. We generated the ac Zeeman shift by applying a current oscillating near ω_0 to generate an off-resonant oscillating magnetic field at the ion. The magnitude of δ_{ac} is proportional to the square of the applied current amplitude I_{ac}, which we verified experimentally by measuring the qubit frequency for different I_{ac} values. We changed I_{ac} between different randomly chosen amplitude values once every millisecond with a switching time of ~1 µs. The time of this change was not synchronized with the rest of the experiment, such that over many experimental trials, the changes will occur at uniformly distributed random times with respect to the start of each trial. The random current amplitudes were chosen to give qubit frequency fluctuations (which cause qubit dephasing) according to a Gaussian distribution with mean value $\bar{\delta}_{ac} = 2\pi \times 4.59(1)$ kHz and standard deviation $\sigma_{ac} = 2\pi \times 0.47(2)$ kHz. The random currents were only applied during the entangling gate.

We characterized the effect of the applied qubit dephasing noise by performing Ramsey experiments as follows. First, the qubits were initialized in the state $|{\downarrow\downarrow}\rangle$. A global carrier $\pi/2$ pulse was then applied to the qubits. Next, the fluctuating ac Zeeman shift was applied for duration t_R. A second carrier $\pi/2$ pulse completed the Ramsey sequence and the two-ion populations were measured. For a given distribution of applied ac Zeeman shift fluctuations, we measured the populations for various values of t_R. We fit these data to a numerical model of the expected populations, computed from an ensemble of simulated trials with random static qubit frequency shifts drawn from a Gaussian distribution. This fit enabled us to determine the mean and standard deviation of the qubit frequency shifts due to the applied ac Zeeman shift noise. We cross-calibrated by measuring δ_{ac} as a function of I_{ac} and calculating the mean and standard deviation of δ_{ac} based on the known distribution of I_{ac} values applied. These two calibrations agreed quantitatively.

Numerical simulations. For numerical simulations of the data obtained in the experiment, we included three types of motional decoherence process: (1) motional dephasing due to the coupling to a phase-damping reservoir[58], (2) shot-to-shot fluctuations of the trap frequency, and (3) motional heating[59]. Dephasing (type 1) can be modelled by the master equation for the system density matrix written as[58]

$$\dot{\hat{\rho}} = \frac{\gamma}{2}\left[2\hat{a}^\dagger\hat{a}\hat{\rho}\hat{a}^\dagger\hat{a} - \left(\hat{a}^\dagger\hat{a}\right)^2\hat{\rho} - \hat{\rho}\left(\hat{a}^\dagger\hat{a}\right)^2\right], \quad (19)$$

where γ is the dephasing rate. In our simulations, we took γ to be a free parameter to fit the experimental data. The motional dephasing terms can be converted into a quantum stochastic equation using the Ito calculus[60] for $\hat{a}$ given by

$$\dot{\hat{a}} = -\frac{\gamma}{2}\hat{a} - i\sqrt{\gamma}\eta(t)\hat{a}, \quad (20)$$

where $\eta(t)$ describes white noise with the correlation $\langle \eta(t+t')\eta(t) = \rangle \delta_D(t')$. Here δ_D is the Dirac delta function. Shot-to-shot motional frequency fluctuations (type 2) are included by running the simulation many times, each time with a randomly chosen motional frequency. The motional frequency values were chosen from a Gaussian distribution with standard deviation of $\sigma_\delta = 2\pi \times 100$ Hz, consistent with the shot-to-shot variation in motional frequency observed experimentally. As we used an out-of-phase motional mode, motional heating (type 3) was strongly suppressed. We measured a heating rate of $\dot{\bar{n}} \approx 1$ quanta per second on this mode, which has a relatively small effect on the gate fidelity. Heating is included phenomenologically using a method similar to the treatment of photon scattering[34].

Quadratic Hamiltonian interaction picture. We performed the numerical simulations for the data in Figs. 2 and 3 in the interaction picture of the quadratic Hamiltonian $\hat{H}_Q(t) = \hat{H}_P - \hat{H}_1$, where $\hat{H}_P$ is the parametric drive Hamiltonian without the rotating wave approximation in equation (7) and $\hat{H}_1 = \hbar\delta\hat{a}^\dagger\hat{a}$. Since $\hat{H}_Q(t)$ is quadratic in $\hat{a}$ and $\hat{a}^\dagger$, the interaction-picture creation operator $\hat{a}_I^\dagger$ is given by

$$\hat{a}_I^\dagger = \hat{U}_Q^\dagger(t)\hat{a}^\dagger\hat{U}_Q(t) = u(t)\hat{a}^\dagger + v^*(t)\hat{a}, \quad (21)$$

where $\hat{U}_Q(t) = \hat{\mathcal{T}}\exp\left(-i\int_0^t \hat{H}_Q(\tau)d\tau\right)$ and $\hat{\mathcal{T}}$ is the time-ordering operator. The equations to determine $u(t)$ and $v(t)$ are given by

$$\begin{aligned}\dot{u} &= \left[-\tfrac{\gamma}{2} - i\left(\delta + \sqrt{\gamma}\eta(t)\right)\right]u + ig\left(e^{i\theta} + e^{-i2\omega_p t - i\theta}\right)v,\\ \dot{v} &= \left[-\tfrac{\gamma}{2} + i\left(\delta + \sqrt{\gamma}\eta(t)\right)\right]v - ig\left(e^{-i\theta} + e^{i2\omega_p t + i\theta}\right)u.\end{aligned} \quad (22)$$

In the interaction picture of $\hat{H}_Q(t)$, the boson-mediated interaction term of equation (1) becomes

$$\begin{aligned}\hat{\mathcal{V}}(t) &= \hat{U}_Q^\dagger(t)\tfrac{\hbar\Omega_0}{2}(\hat{S}^\dagger\hat{a} + \hat{S}\hat{a}^\dagger)\hat{U}_Q(t)\\ &= \hbar\tfrac{\Omega_0}{2}\left(\hat{S}^\dagger h^*(t)\hat{a} + \hat{S}h(t)\hat{a}^\dagger\right),\end{aligned} \quad (23)$$

where $h(t) = u(t) + v(t)$ and $\hat{S} = \hat{\sigma}_x^1 - \hat{\sigma}_x^2$. For example, without the parametric drive and the motional dephasing, $h(t) = e^{-i\delta t}$. As the interaction Hamiltonian $\hat{\mathcal{V}}(t)$ is only linear in $\hat{a}$ and $\hat{a}^\dagger$, the qubit-motion system can be written as

$$\begin{aligned}|\Psi(t)\rangle &= c_{++}(t)\,|{++}\rangle\,|\alpha_{++}(t)\rangle\\ &+ c_{+-}(t)\,|{+-}\rangle\,|\alpha_{+-}(t)\rangle\\ &+ c_{-+}(t)\,|{-+}\rangle\,|\alpha_{-+}(t)\rangle\\ &+ c_{--}(t)\,|{--}\rangle\,|\alpha_{--}(t)\rangle,\end{aligned} \quad (24)$$

where $c_{\pm\pm}(t)$ are time-dependent coefficients for the qubit states $|{\pm\pm}\rangle$ and the $|\alpha_{\pm\pm}(t)\rangle$ are coherent states of motion defined by $|\alpha_{\pm\pm}(t)\rangle = \hat{\mathcal{D}}(\alpha_{\pm\pm}(t))\,|0\rangle$, where $\hat{\mathcal{D}}(\alpha) = \exp\left(\alpha\hat{a}^\dagger - \alpha^*\hat{a}\right)$ is the displacement operator[7]. In the eigenbasis of $\hat{S}$, we find $\alpha_{++}(t) = \alpha_{--}(t) = 0$ and $\alpha_{+-}(t) = -\alpha_{-+}(t) = -i\int_0^t \Omega_0 h(t')dt'$. With the initial qubit state $|{\downarrow\downarrow}\rangle$ and the target state $|\psi_B\rangle = \frac{1}{\sqrt{2}}(|{\downarrow\downarrow}\rangle + i\,|{\uparrow\uparrow}\rangle)$, the fidelity at the gate time τ can be evaluated as

$$F(\tau) = \left|\frac{1}{2} - ic_{+-}(\tau)\exp\left(-|\alpha_{+-}(\tau)|^2/2\right)\right|^2. \quad (25)$$

We can then find the optimal fidelity with respect to the gate time τ for fixed δ and g. In the simulations of Figs. 2 and 3, we averaged the optimal fidelity over 600 simulations for each value of g. In each simulation, we drew a random motional frequency shift from a zero-mean Gaussian distribution with the standard deviation $\sigma_\delta = 2\pi \times 100$ Hz. Every simulation had the same value of the motional dephasing rate γ. We determined $\gamma \approx 2\pi \times 5.2$ Hz by fitting the fidelity simulations to the data.

Amplified motional dephasing. Parametric modulation amplifies decoherence of the bosonic mode resulting in the loss of fidelity of boson-mediated interactions. Here we derive expressions for the impact on the fidelity of amplified motional dephasing due to coupling to a phase-damping reservoir.

In the absence of parametric amplification, the contribution to the system Hamiltonian from dephasing is given by

$$\hat{H}_d = \hbar\sqrt{\gamma}\eta(t)\hat{a}^\dagger\hat{a} \quad (26)$$

where $\langle \eta(t+t')\eta(t) = \rangle \delta_D(t')$. For a dephasing rate of $\gamma = 2\pi \times 5.2$ Hz, and a gate duration of 342 µs without parametric amplification, the variance of the phase fluctuation is $\langle \Delta\phi^2 \rangle = \gamma t = 0.0112$ rad^2 or $\sqrt{\langle \Delta\phi^2 \rangle} = 6.06$ degrees. Thus, the loss in fidelity for a MS gate using our experimental parameters is determined through the phase fluctuation variance to be ~0.7%[61]. To estimate the effect on the fidelity of a two-qubit gate in the presence of parametric amplification, we applied the Bogoliubov transformation $\hat{a} = \hat{b}\cosh r + \hat{b}^\dagger \sinh r$ at $\theta = 0$ so that

$$\hat{H}_d \to \hbar\sqrt{\gamma}\eta(t)\left[\cosh(2r)\hat{b}^\dagger\hat{b} + \cosh r \sinh r(\hat{b}^2 + \hat{b}^{\dagger 2})\right], \quad (27)$$

dropping a constant term. The term proportional to $(\hat{b}^2 + \hat{b}^{\dagger 2})$ produces a random squeezing that is negligibly weak in the regime $\delta' \gg \gamma$ where we operate, and can be ignored. The remaining term shows that the dephasing rate is amplified by a factor of $[\cosh(2r)]^2 = \left(G^2 + G^{-2}\right)^2/4$, which is approximately $G^4/4$ for large G. The variance of the dephasing angle is amplified by $G^4/4 \times G^{-1} = G^3/4$, where the factor of G^{-1} results from the reduction in gate time. Since the loss of fidelity is

proportional to the phase fluctuation variance[61], for $G=3.25$ at $g=2\pi\times50$ kHz, the fidelity loss is estimated to be ~6%, a factor of $G^3/4\approx8.6$ higher than without amplification.

ac Zeeman shift fluctuations. To show the robustness of the parametric amplification against fluctuations of the qubit frequency as shown in Fig. 2b (red data points and shaded band), we introduced artificial qubit frequency fluctuations by applying a detuned oscillating current to one of the trap electrodes, as described above. The detuned current induces an ac Zeeman shift, whose magnitude is randomly varied by changing the current amplitude every millisecond to give a Gaussian distribution of qubit frequencies. Effectively, we add an additional term $\hat{H}_z=\hbar\frac{\delta_{ac}}{2}(\hat{\sigma}_z^1+\hat{\sigma}_z^2)$ to the system Hamiltonian, where δ_{ac} is drawn from a Gaussian distribution with mean $\bar{\delta}_{ac}=2\pi\times4.59(1)$ kHz and standard deviation $\sigma_{ac}=2\pi\times0.47$ kHz. In this case, the state cannot be written in the form of equation (24) due to the fact that $\left[\hat{H}_z,\hat{S}\right]\neq0$ for $\hat{S}=\hat{\sigma}_x^1-\hat{\sigma}_x^2$. Instead, we write the state of the whole system as

$$|\Psi(t)\rangle=\sum_{j=1}^{3}\sum_{k=0}^{s}C_{j,k}(t)\left|\psi_j\right\rangle|k\rangle, \tag{28}$$

where $|k\rangle$ is the kth Fock state of motion, $|\psi_1\rangle=\frac{1}{\sqrt{2}}(|{+}{+}\rangle+|{-}{-}\rangle)$, $|\psi_2\rangle=\frac{1}{\sqrt{2}}(|{+}{-}\rangle+|{-}{+}\rangle)$, $|\psi_3\rangle=\frac{1}{\sqrt{2}}(|{+}{-}\rangle-|{-}{+}\rangle)$ and $|\Psi(0)\rangle=\frac{1}{\sqrt{2}}(|\psi_1\rangle-|\psi_2\rangle)|0\rangle$. The other eigenstate $|\psi_0\rangle=\frac{1}{\sqrt{2}}(|{+}{+}\rangle-|{-}{-}\rangle)$ of the two-qubit system is not involved because it is a dark state of the operators $\hat{H}_z$ and $\hat{S}$ and it is orthogonal to the initial state $|{\downarrow}{\downarrow}\rangle$. The set of equations is truncated at a certain motional Fock state $|s\rangle$ depending on the maximum displacement of the motional state $|\alpha_{max}|\equiv\left|\int_0^{\tau/2}\Omega_0h(t')\mathrm{d}t'\right|$. According to the Schrödinger equation under the Hamiltonian $\hat{H}_z+\hat{\mathcal{V}}(t)$, the differential equations of the coefficients are obtained as

$$\begin{aligned}\dot{C}_{1,k}&=-i\delta_{ac}C_{2,k},\\ \dot{C}_{2,k}&=-i\delta_{ac}C_{1,k}-i\Omega_0\left(C_{3,k+1}h^*\sqrt{k+1}+C_{3,k-1}h\sqrt{k}\right),\\ \dot{C}_{3,k}&=-i\Omega_0\left(C_{2,k+1}h^*\sqrt{k+1}+C_{2,k-1}h\sqrt{k}\right).\end{aligned} \tag{29}$$

The fidelity at the gate time is then given by

$$F(\tau)=\frac{1}{2}|C_{1,0}(\tau)-iC_{2,0}(\tau)|^2. \tag{30}$$

For example, at the maximum $g\sim2\pi\times50$ kHz, the maximum displacement is $|\alpha_{max}|\approx3$, and we verified that the truncation number $s=23$ is sufficient. For Fig. 2b, we averaged the optimal fidelity over 600 runs of simulations for each value of g, where both the motional frequency and the ac Zeeman shift were randomly chosen in each simulation.

The above analysis can be extended to an initial thermal state of the mechanical mode, where $\hat{\rho}_m(0)=\sum_{n=0}^{\infty}p_n|n\rangle\langle n|$ and $p_n=\bar{n}^n/(\bar{n}+1)^{n+1}$. The density matrix of the whole system is written as

$$\hat{\rho}(t)=\sum_{n=0}^{\infty}p_n|\Psi_n(t)\rangle\langle\Psi_n(t)|, \tag{31}$$

where

$$|\Psi_n(t)\rangle=\sum_{j=1}^{3}\sum_{k=0}^{s}C_{j,k,n}(t)\left|\psi_j\right\rangle|k\rangle \tag{32}$$

and the coefficients $C_{j,k,n}$ follow the same differential equations as $C_{j,k}$ in equation (29) with the initial conditions $C_{1,k,n}(0)=-C_{2,k,n}(0)=\delta_{k,n}$. Here $\delta_{k,n}$ is the Kronecker delta. The fidelity for the target state after tracing over the motional mode is then generalized to

$$F(\tau)=\frac{1}{2}\sum_{n=0}^{\infty}p_n\sum_{k=0}^{\infty}|C_{1,k,n}(\tau)-iC_{2,k,n}(\tau)|^2. \tag{33}$$

The role of thermal excitation in affecting the fidelity in this case can be understood in the following way. First, without ac Zeeman shift fluctuations, the thermal excitation does not affect the fidelity at the ideal gate time. This is also true with parametric amplification thanks to the mapped Hamiltonian equation (3).

Second, in the presence of an ac Zeeman shift ($\delta_{ac}\neq0$), there can be residual spin-motion entanglement due to the coupling between spin states $|\psi_1\rangle$ and $|\psi_2\rangle$, even at the ideal gate time. With parametric amplification, this coupling rate δ_{ac} is effectively suppressed since the value of $|h|$ is increased from 1 to a value greater than 1 in equation (29). This suppression works for any motional state in the thermal excitation according to our analysis. Therefore, the parametric amplification would help reduce the effects of qubit dephasing on fidelity even with an initial thermal state of the motional mode. This was demonstrated in our experiments (Fig. 2b).

Data availability

Source data are provided with this paper. All other data that support the plots within this paper and other findings of this study are available from the corresponding authors upon reasonable request.

Code availability

The simulation and analysis codes are available from the corresponding authors upon reasonable request.

References

54. Wineland, D. J. et al. Experimental issues in coherent quantum-state manipulation of trapped atomic ions. *J. Res. Natl Inst. Stand. Technol.* **103**, 259–328 (1998).
55. Heinzen, D. J. & Wineland, D. J. Quantum-limited cooling and detection of radio-frequency oscillations by laser-cooled ions. *Phys. Rev. A* **42**, 2977–2994 (1990).
56. Walls, D. F. & Milburn, G. J. *Quantum Optics* (Springer-Verlag, 1994).
57. Tellinghuisen, J. Statistical error propagation. *J. Phys. Chem. A* **105**, 3917–3921 (2001).
58. Turchette, Q. A. et al. Decoherence and decay of motional quantum states of a trapped atom coupled to engineered reservoirs. *Phys. Rev. A* **62**, 053807 (2000).
59. Brownnutt, M., Kumph, M., Rabl, P. & Blatt, R. Ion-trap measurements of electric-field noise near surfaces. *Rev. Mod. Phys.* **87**, 1419–1482 (2015).
60. Gardiner, C. W., Parkins, A. S. & Zoller, P. Wave-function quantum stochastic differential equations and quantum-jump simulation methods. *Phys. Rev. A* **46**, 4363–4381 (1992).
61. Sepiol, M. *A High-Fidelity Microwave Driven Two-Qubit Quantum Logic Gate in $^{43}Ca^+$*. PhD thesis, Univ. Oxford (2016).

Acknowledgements

We thank R. W. Simmonds, J. Schmidt and L. J. Stephenson for a careful reading of the manuscript. These experiments were performed using the ARTIQ control system. At the time the work was performed, S.C.B., R.S., H.M.K. and D.T.C.A. were Associates in the Professional Research Experience Program (PREP) operated jointly by NIST and the University of Colorado. This work was supported by the NIST Quantum Information Program.

Author contributions

S.C.B. carried out the experiments with assistance from D.H.S., R.S., H.M.K. and D.T.C.A., based on protocols developed by W.G. and J.J.B. D.T.C.A., D.H.S., R.S., S.C.B. and H.M.K. built and maintained the apparatus. S.C.B., H.M.K., W.G. and D.H.S. analysed the data and performed simulations. S.C.B. wrote the manuscript with input from all authors. D.H.S. supervised the work, with support from J.J.B., D.T.C.A., D.L., A.C.W. and D.J.W.

Competing interests

The authors declare no competing interests.

Additional information

Extended data is available for this paper at https://doi.org/10.1038/s41567-021-01237-9.

Correspondence and requests for materials should be addressed to S.C.B. or D.H.S.

Peer review information *Nature Physics* thanks the anonymous reviewers for their contribution to the peer review of this work.

Reprints and permissions information is available at www.nature.com/reprints.

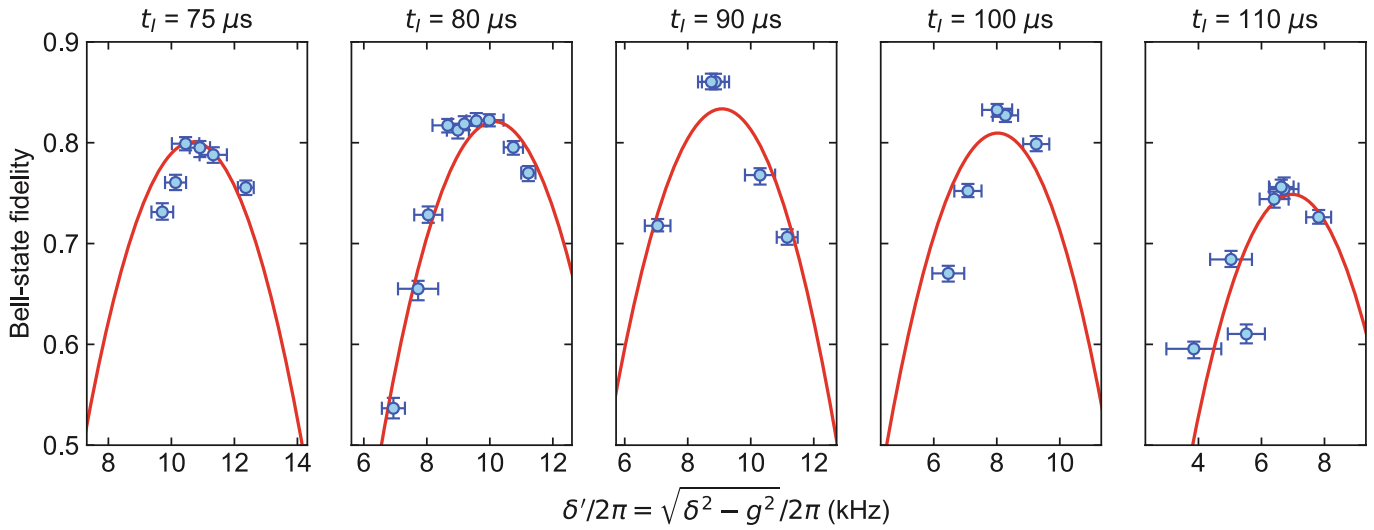

Extended Data Fig. 1 | Data and fitting to determine $\tilde{t}_{l,est}$. Fidelity as a function of $\delta'/2\pi$ for various values of t_l for a calibrated value of the parametric coupling strength of $g/2\pi = 49.7(6)$ kHz. Data points are fidelities obtained using the method described in ref. [46]. Vertical error bars indicate 68% confidence intervals for the fidelity. Horizontal error bars indicate 68% confidence intervals for $\delta'/2\pi$ calculated from error propagation of the measured uncertainties in δ and g within a given experiment. Red curves are slices of the 2D quadratic fitting function at the corresponding interaction times.